WIND
ENERGY
SCIENCE

eawe
european academy of wind energy

Open Access

Wind turbine power production and annual energy production depend on atmospheric stability and turbulence

Clara M. St. Martin[1], **Julie K. Lundquist**[1,2], **Andrew Clifton**[2], **Gregory S. Poulos**[3], and **Scott J. Schreck**[2]

[1]Department of Atmospheric and Oceanic Sciences (ATOC), University of Colorado at Boulder, 311 UCB, Boulder, CO 80309, USA
[2]National Renewable Energy Laboratory, 15 013 Denver West Parkway, Golden, CO 80401, USA
[3]V-Bar, LLC, 1301 Arapahoe Street, Suite 105, Golden, CO 80401, USA

Correspondence to: Clara M. St. Martin (clara.st.martin@colorado.edu)

Abstract. Using detailed upwind and nacelle-based measurements from a General Electric (GE) 1.5sle model with a 77 m rotor diameter, we calculate power curves and annual energy production (AEP) and explore their sensitivity to different atmospheric parameters to provide guidelines for the use of stability and turbulence filters in segregating power curves. The wind measurements upwind of the turbine include anemometers mounted on a 135 m meteorological tower as well as profiles from a lidar. We calculate power curves for different regimes based on turbulence parameters such as turbulence intensity (TI) as well as atmospheric stability parameters such as the bulk Richardson number (R_B). We also calculate AEP with and without these atmospheric filters and highlight differences between the results of these calculations. The power curves for different TI regimes reveal that increased TI undermines power production at wind speeds near rated, but TI increases power production at lower wind speeds at this site, the US Department of Energy (DOE) National Wind Technology Center (NWTC). Similarly, power curves for different R_B regimes reveal that periods of stable conditions produce more power at wind speeds near rated and periods of unstable conditions produce more power at lower wind speeds. AEP results suggest that calculations without filtering for these atmospheric regimes may overestimate the AEP. Because of statistically significant differences between power curves and AEP calculated with these turbulence and stability filters for this turbine at this site, we suggest implementing an additional step in analyzing power performance data to incorporate effects of atmospheric stability and turbulence across the rotor disk.

1 Introduction

Power performance testing and annual energy production (AEP) assessments rely on accurate calculations of wind turbine power curves. Previous work on power performance highlights the role of turbulence intensity (TI) and wind shear in influencing power production (Elliot and Cadogan, 1990; Hunter et al., 2001; Kaiser et al., 2003; Sumner and Masson, 2006; Gottschall and Peinke, 2008; Antoniou et al., 2009; Rareshide et al., 2009; Wharton and Lundquist, 2012a, b; Clifton et al., 2013a; Dörenkämper et al., 2014). Wharton and Lundquist (2012b) also found that vertical TI and tur-

bulence kinetic energy (TKE) affect power performance and Rareshide et al. (2009) found that veer affects power performance. Atmospheric stability induces deviations of power from the manufacturer power curve (MPC) (Motta et al., 2005; van den Berg, 2008; Vanderwende and Lundquist, 2012; Wharton and Lundquist, 2012b), and atmospheric variations across the rotor disk can influence power performance results (Sumner and Masson, 2006; Wagner et al., 2009; Choukulkar et al., 2016).

Because the power curve so closely impacts AEP, factors that influence power performance typically influence AEP calculations as well. As suggested by the works mentioned

above, the two most closely explored atmospheric factors with regard to AEP are TI and wind shear, but the existing studies do not agree on the influence of TI and wind shear on AEP. The simulation-based study of Antoniou et al. (2009) found that low wind shear supported high AEP. For low wind speeds, the highest AEP occurred during conditions of high TI, but at higher wind speeds, the highest AEP occurred when TI was low. In contrast, based on data from a number of wind farms in the continental US, Rareshide et al. (2009) also compared AEP calculated with different TI and shear combinations, and found that AEP typically decreased with increasing TI, but increased with increasing shear.

In this study, we also investigate the influence of different atmospheric stability and turbulence regimes on wind turbine power curves and AEP calculations, incorporating a broad set of atmospheric parameters as well as different approaches to measuring these parameters. In Sect. 2 we describe our data set, which includes an upwind meteorological (met) tower with measurements spanning the rotor disk as well as a wind-profiling lidar. In Sect. 3 we present our data analysis methods, which include filtering the data by atmospheric parameters like shear, TI, and atmospheric stability. The effects of atmospheric parameters on power curves and AEP are presented in Sect. 4, and in Sect. 5 we summarize conclusions about the effects of atmospheric stability and inflow turbulence on power curves and AEP calculations.

2 Data

2.1 Measurement site

The measurements used in this analysis were collected at the US Department of Energy (DOE) National Wind Technology Center (NWTC, Fig. 1) at the National Renewable Energy Laboratory (NREL), located just south of Boulder, Colorado, and about 5 km east of the Colorado Front Range (Clifton et al., 2013b; Aitken et al., 2014). The prevailing wind direction at 80 m (hub height) at this site during this campaign (29 November 2012–14 February 2013) was west-northwesterly.

This wind direction also dominated a 14-year period from a neighboring met tower at the NWTC (Clifton and Lundquist, 2012). During the winter, the downslope flow from the nearby Rocky Mountains is frequently channeled through Eldorado Canyon, located just west-northwest of the NWTC (Banta et al., 1996; Poulos et al., 2000, 2007; Clifton et al., 2013b; Aitken et al., 2014). The NWTC site slopes upward with about 20 m in elevation change toward the west for about 1.5 km before dropping off 20 m towards the highway on the western edge of the site. The surface is mostly short grass.
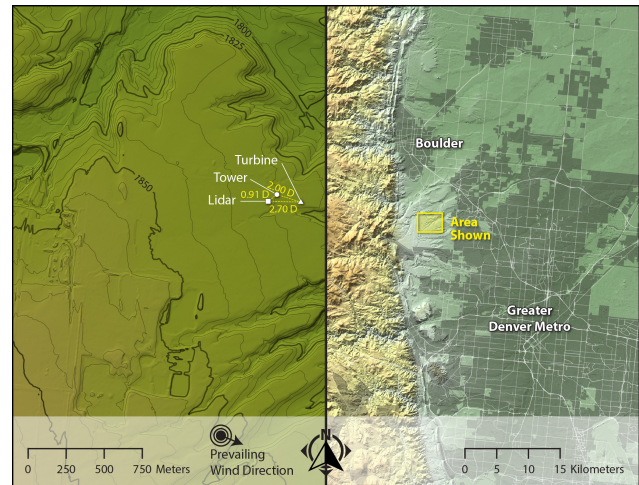

Figure 1. Left panel: local map of the NWTC with instrument locations and topographic contours in meters above sea level. Right panel: the regional setting of the NWTC between the greater Denver metropolitan area and Boulder, with the Front Range of the Rocky Mountains shown in the higher topography west of the site. (Courtesy of Joshua Bauer and Billy Roberts at NREL.)

2.2 Upwind measurements

Upwind measurements were taken using a Renewable NRG Systems (NRG)/LEOSPHERE WINDCUBE v1 vertically profiling Doppler lidar (Courtney et al., 2008; Rhodes and Lundquist, 2013) and a 135 m met tower. The tower supports several levels of cup anemometers, vanes, sonic anemometers, and temperature sensors, along with precipitation and air-pressure sensors (Fig. 2, Table 1) all on booms pointing in the dominant wind direction (west-northwest). Data were collected during the winter season, typically the season of the strongest winds at the NWTC (from 29 November 2012 through 14 February 2013). The lidar is located about 216 m (2.7 D) west of the General Electric (GE) 1.5sle turbine on the NWTC site. The met tower is located approximately 160 m (2.0 D) west-northwest of the turbine (Fig. 1). Because different instruments employ different averaging methods, Fig. 3 demonstrates that all wind speed data sets were synchronized and illustrates how the power output responds to changes in wind speed.

2.2.1 Lidar

The NRG/LEOSPHERE WINDCUBE v1 lidar measures volumetric-averaged wind speeds and directions every 20 m from 40 to 220 m, thereby spanning the entire vertical extent of the turbine rotor disk. The wind speeds are measured with an accuracy of $0.2\,\mathrm{m\,s^{-1}}$ and the wind directions are measured with an accuracy of 1.5° (Courtney et al., 2008). First, we filtered the nominally 1 Hz measurements of the horizontal wind speeds and directions for suitable carrier-to-noise ratio (CNR). Next, we averaged these 1 Hz data to 10 min av-

Table 1. 135 m met tower instrument information.

Type	Instrument	Mounting heights (m)	Accuracy
Cup anemometer	Met One SS-201	3, 10, 38, 87, 122	$0.5\,\mathrm{m\,s^{-1}}$
Cup anemometer	Thies 4.3351.10.0000	30, 55, 80, 105, 130	$0.2\,\mathrm{m\,s^{-1}}$
Wind vane	Met One SD-201	3, 10, 38, 87, 122	$3.6°$
Air temperature sensor	Met One T-200A platinum RTD	3, 38, 87	$0.1\,°\mathrm{C}$
Differential temperature sensor	Met One T-200A	38, 87, 122	$0.1\,°\mathrm{C}$
Sonic anemometer	ATI "K" type	15, 41, 61, 74, 100, 119	$0.01\,\mathrm{m\,s^{-1}}$
Boom triaxial acceleration sensor	Summit 34201A	15, 41, 61, 74, 100, 119	
Sonic temperature	ATI "K" type	15, 41, 61, 74, 100, 119	$0.1\,°\mathrm{C}$
Barometric pressure sensor	AIR AB-2AX	3	
Dew point temperature sensor	Therm-x 9400ASTD	3, 38, 87, 122	
Precipitation sensor	Vaisala DRD11A	3	
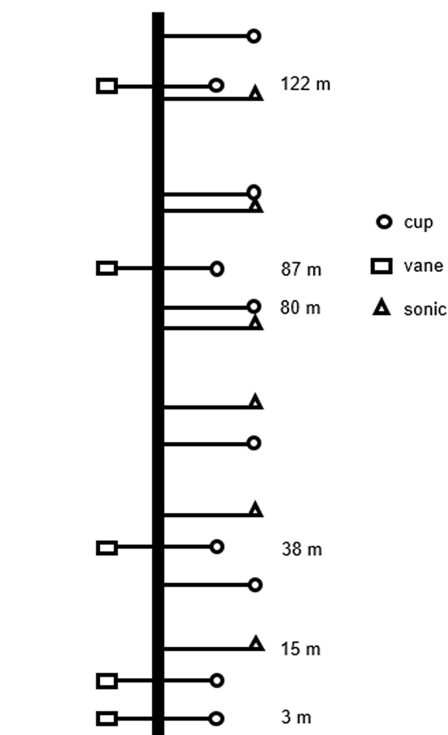
Figure 2. Configuration of 135 m meteorological tower with some key heights labeled. This tower varies slightly from the M4 tower described in Clifton et al. (2013b), but data are available online (NWTC, 2016).

erages for comparison with the tower and turbine data. The lidar takes a volumetric measurement, assuming homogeneity over the entire volume it is measuring. This process introduces an uncertainty in the lidar measurements in inhomogeneous flow (Bingöl et al., 2009; Rhodes and Lundquist, 2013; Lundquist et al., 2015); this possible source of error is discussed in further detail in the Supplement (Sect. S1).

2.2.2 Meteorological tower

The M5 met tower (NWTC, 2016, similar to the M4 tower at the site, which was studied by Rinker et al., 2016) is instrumented with cup anemometers at 3, 10, 30, 38, 55, 80, 87, 105, 122, and 130 m, and vanes at 3, 10, 38, 87, and 122 m (Fig. 2 and Table 1). Barometric pressure and precipitation sensors are located at 3 m and temperature sensors at 3, 38, and 87 m (Table 1). Sonic anemometers are mounted at 15, 41, 61, 74, 100, and 119 m (Fig. 2 and Table 1). The tower booms are directed at 278°, into the prevailing wind direction, slightly north of west. Measurements from the sonic anemometers at 15 and 74 m are used to calculate turbulent fluxes of momentum and heat for assessment of atmospheric stability and turbulence as discussed in the following sections.

2.3 Wind turbine data

A GE 1.5 MW turbine (GE 1.5/77 sle) with an 80 m hub height was chosen for this study. The GE 1.5 MW is the most widely deployed utility-scale turbine in the world with more than 12 000 turbines deployed around the globe as of 2009 (GE Energy, 2009). The supervisory control and data acquisition (SCADA) system of the turbine provides 10 min averages of nacelle wind speed, nacelle orientation, turbine power, blade pitch angles, and generator speed set point. These measurements can be compared with the upwind measurements to quantify power curves and AEP. The cup anemometer mounted on the nacelle of the turbine is a NRG IceFree Hybrid XT turbine control anemometer. The GE 1.5sle reaches its nameplate capacity, 1.5 MW, at a wind speed of 14 m s^{-1} (GE Energy, 2009). We refer to this wind speed as the rated wind speed for the rest of this article. The lower and upper extremes of the swept area of the GE 1.5sle in this study are approximately 41.5 and 118.5 m above ground. More details on this turbine and power performance testing results as well as instrument and site calibration information can be found in Mendoza et al. (2015).
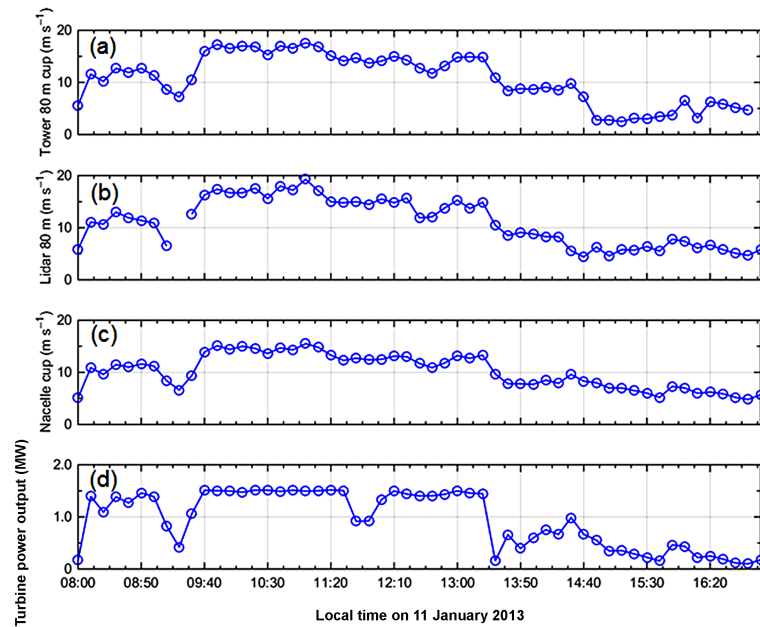
Figure 3. Time series from 11 January 2013 from 08:00 to 17:00 MST (Mountain Standard Time): **(a)** is a time series of 80 m wind speeds measured by the cup on the tower, **(b)** is a time series of 80 m wind speeds measured by the lidar, **(c)** is a time series of the hub-height wind speeds measured by the cup anemometer on the nacelle, and **(d)** is a time series of the power output from the turbine.

3 Analysis methods

Before calculating atmospheric parameters, all meteorological and turbine data are checked for data quality as described in Sect. 3.1.

3.1 Data quality control

3.1.1 Lidar

All lidar-measured wind speed measurements are filtered by CNR: only measurements with a CNR greater than -18 dB are retained. Lower CNR results from clean-air conditions (Aitken et al., 2012), which occur frequently on Colorado's Front Range in the winter. After additional filtering for quality-control purposes (such as removing bad data as defined by the manufacturer's wind speed and temperature limits), the data recovery rate is approximately 33.5 % for horizontal wind speeds and directions at 40 m, 40 % for horizontal wind speeds and directions at 60 and 120 m, and 45 % for horizontal wind speeds and directions at 80 and 100 m.

3.1.2 Meteorological tower

Quality control filtering methods performed on the met tower data discard data that are flagged for a number of reasons, including irregular timing (the time between measurements is inconsistent), insufficient percentage of data points within an averaging period (less than 95 %), low standard deviation (less than 0.01 % of the mean) or constant values during the

measurement interval (which indicate icing events), empty data channels, bad values as defined by manufacturer limits, or when an instrument records a "NaN" in place of a real measurement. After filtering for quality-control purposes, the met tower provides horizontal wind speeds and directions and temperatures about 90 % of the time at all levels during this study.

Several spikes in wind speed occur in the raw sonic anemometer data. Therefore, a de-spiking filter is applied based on the change in wind speed from each data point to the next. Data points are removed if they are preceded and followed by changes exceeding the lowest 99 % of all changes. After filtering the spikes in the sonic anemometers as well as the previously discussed quality-control procedure, the sonic anemometers provide wind speed and temperature about 90 % of the time at 15 m and about 60 % at 74 m during this study.

3.2 Wind speed and direction subselection

Although the dominant wind direction at the site is west-northwesterly, other wind directions do occur. To ensure the lidar and met tower measurements are upwind of the turbine, we consider only data from time periods of hub-height wind from the 235–315° wind direction sector. This sector includes the most frequent and highest wind speeds as measured by both upwind instruments (Fig. 4). Only wind speeds between cut-in ($3.5 \, \mathrm{m \, s^{-1}}$) and cut-out ($25 \, \mathrm{m \, s^{-1}}$) are considered to ensure that the turbine is operating.
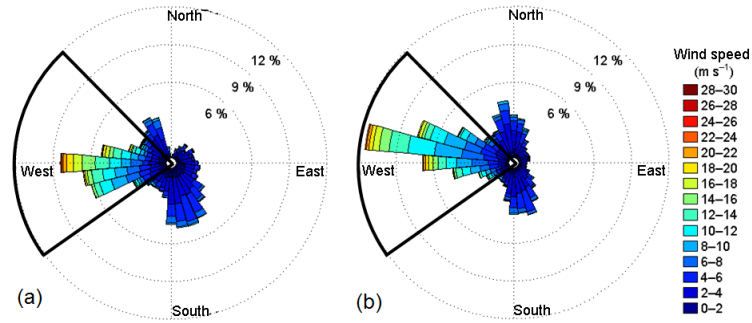
Figure 4. Wind roses for **(a)** lidar 80 m altitude and **(b)** met tower 87 m altitude, the closest to hub-height with both a cup and vane. Wind speed bins are $2\,\mathrm{m\,s^{-1}}$ and wind directions bins are $10°$. The black outline highlights the chosen wind direction sector.
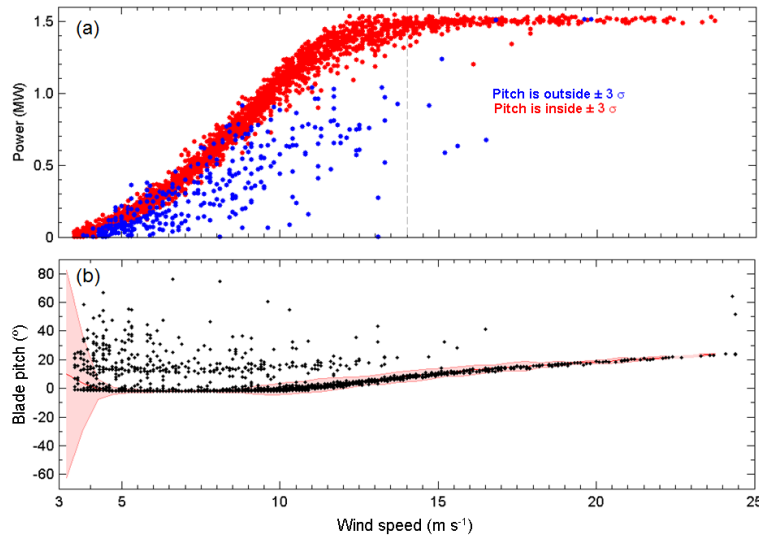

Figure 5. (a) Scatter power curve based on the tower 80 m wind speed. Blue dots show points that are outside of the median absolute deviation (MAD) envelope in **(b)** and the red dots represent points that are within the MAD envelope in **(b)**. The vertical grey dashed line marks rated speed. **(b)** Blade pitch angle from a single blade vs. tower 80 m wind speed. Red envelope represents $\pm4.5\,\mathrm{MAD}$ of the blade pitch angle within wind speed bins $0.5\,\mathrm{m\,s^{-1}}$ wide.

3.3 Filtering turbine underperformance

After filtering for quality control as well as wind speed and direction, a large number of times occur when the turbine is producing significantly less power than expected – underperforming – as seen in Fig. 5a. We test two methods to isolate and discard the cases where the turbine is producing significantly lower power, inconsistent with "normal operation". The first approach relies on blade pitch angle to segregate data and flag most of these underperforming periods; this approach could be used by wind plant owner-operators with access to limited SCADA parameters. When more SCADA parameters are available, such as generator speed set point, these values may be used in a more rigorous way to filter on curtailment and to define normal turbine operation.

3.3.1 Filtering based on blade pitch angle

Without access to the turbine control system or data more refined than 10 min averages, typical blade pitch angles can be quantified as a function of wind speed (Fig. 5b). The median value for blade pitch angle for each wind speed bin as well as $\pm4.5\,\mathrm{MAD}$ (median absolute deviation), equivalent to 3σ, are shown by the red envelope in Fig. 5b. (We use MAD here instead of mean absolute deviation so that the calculation is not biased by a few outliers.) When plotted on a power curve using the tower 80 m cup anemometer for wind speed (Fig. 5a), the majority of the points outside of the $\pm4.5\,\mathrm{MAD}$ envelope and between 5 and $17\,\mathrm{m\,s^{-1}}$ show underperformance. To identify underperformance, then, we calculate MAD blade pitch angles from each blade for each wind speed bin between 5 and $17\,\mathrm{m\,s^{-1}}$. Time periods with blade pitch angles outside of $\pm4.5\,\mathrm{MAD}$ are discarded. While variability

on timescales shorter than 10 min may affect turbine operation, the effective filtering seen in the red scatter in Fig. 5a suggests that this approach is sufficient. This filtering by blade pitch angle also has the advantage of using only data to which a typical wind plant operator would have access.

After filtering for hub-height wind speed and direction, positive power production, and blade pitch angle, 1240 out of 7949 lidar 80 m wind speed data points remain (16 %), and 2235 out of 9918 met tower 80 m wind speed data points remain (23 %). Concurrent lidar, met tower, and turbine data that fulfill the various screening criteria occur during 1107 10 min periods.

3.3.2 Filtering based on extensive SCADA turbine operational parameters

Access to a number of turbine control parameters from the SCADA on the DOE GE 1.5sle allows for a more accurate definition of normal turbine operation, mostly based on generator speed set point filtered on curtailment. However, from cut-in wind speed until around $5.5 \, \mathrm{m \, s^{-1}}$, using generator speed set point to filter the data results in discarding too many data points. Therefore, between cut-in wind speed and about $5.5 \, \mathrm{m \, s^{-1}}$, the generator speed set point is not used; rather, data points are discarded only when the turbine is not grid connected and is faulted. Above $5.5 \, \mathrm{m \, s^{-1}}$, only generator speed set point is used to filter on curtailment and for normal operation. The data points filtered using this method are represented in Fig. 6 in blue, while the red points in Fig. 6 represent the data points that pass this filtering method.

After filtering for hub-height wind speed and direction, positive power production, and normal turbine operation, 1227 out of 7949 lidar 80 m wind speed data points remain (15 %), and 2249 out of 9918 met tower 80 m wind speed data points remain (23 %). Concurrent lidar, met tower, and turbine data that fulfill the various screening criteria occur during 1127 10 min periods.

3.3.3 Comparison of different turbine operation filters

The turbine operation filters described in Sect. 3.3.2 not only filter out all of the times when the turbine is producing significantly less power than expected but also allow the use of about 2 % more data points deemed "bad" by the blade pitch angle filtering method described in Sect. 3.3.1. Many of the data points that would be discarded using the blade pitch angle filtering method are between cut-in wind speed and $10 \, \mathrm{m \, s^{-1}}$ and lie reasonably within the expected power curve, on top of data points that passed through the filter. Therefore, the remaining analysis is based on data filtered using the methodology described in Sect. 3.3.2.
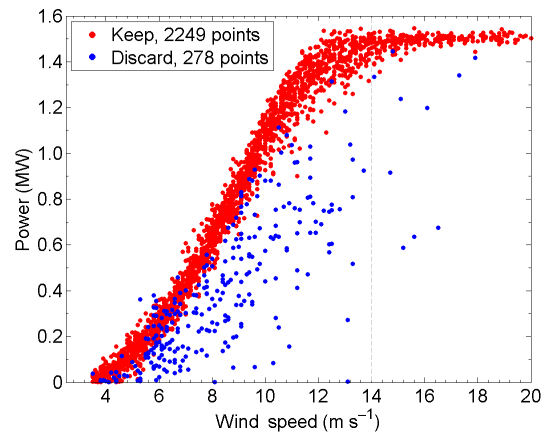

Figure 6. Scatter power curve using the tower 80 m wind speed. Blue dots show points filtered out using turbine control parameters described in Sect. 3.3.2. Red dots show data points that passed this filtering process. The grey dashed line marks rated speed.

3.4 Power curves

Power curves based on wind speeds normalized by air density following the International Electrotechnical Commission (IEC 61400-12-1, 2015) can be used to evaluate turbine performance. The observed power curves, comparing power production to 80 m tower anemometer wind speeds (Fig. 7a), 80 m lidar wind speeds (Fig. 7b), and nacelle anemometer wind speeds (Fig. 7c), generally show good agreement with an approximation of the MPC (GE Energy, 2009). This approximated MPC is determined by placing the publicly available MPC for the GE 1.5sle on a grid (with dimensions of $0.5 \, \mathrm{m \, s^{-1}}$ by 50 kW) and estimating expected power produced at each wind bin.

The nacelle-mounted anemometer does not observe the ambient wind speed that the rotor disk experiences because the wind that flows through the rotor disk and along the nacelle during operation is modified by the blades and nacelle (Antoniou and Pedersen, 1997; Smith et al., 2002; Frandsen et al., 2009; Zahle and Sørensen, 2011). However, power curves calculated using nacelle wind speeds are shown here along with power curves calculated using upwind measurements in order to compare the different methods. In many cases, operators calculate these nacelle-based power curves due to lack of other data.

The power curves created from 10 min tower and nacelle-mounted anemometer measurements (Fig. 7a and c, respectively) show less variability than the lidar power curve (Fig. 7b). It is especially apparent from the power curve created from 10 min lidar measurements (Fig. 7b) that the lidar variability at this particular site is vulnerable to inhomogeneity in the flow. Although lidars are widely available and used in the field (Clifton, 2015), the variability between the lidar and tower measurements (Fig. 8) indicates sufficient inhomogeneity in the flow at this particular site (as observed by
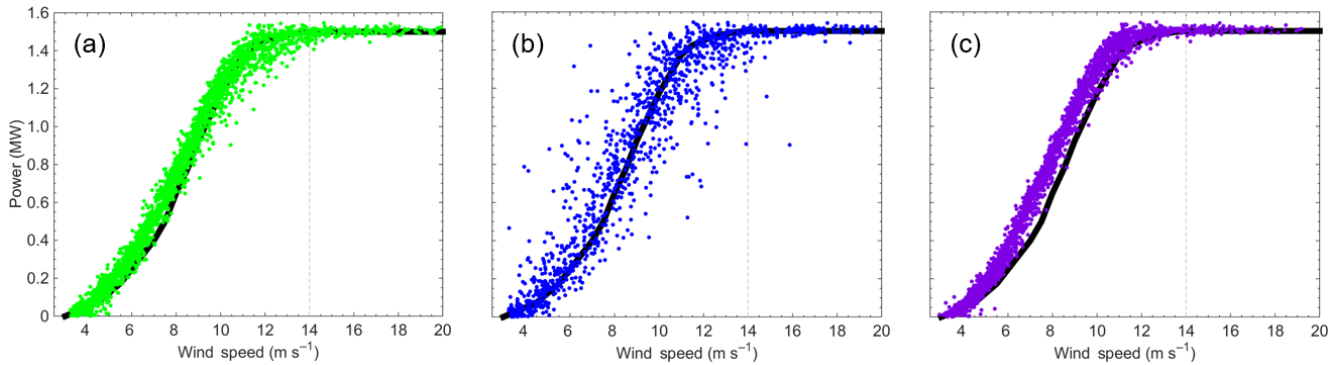
Figure 7. Power curves after filtering for wind speeds between 3.5 and 25 m s^{-1}, wind directions between 235 and 315°, and for normal turbine operation: **(a)** turbine power production vs. 80 m cup anemometer wind speed from the met tower, **(b)** turbine power production vs. 80 m wind speed from the lidar, and **(c)** turbine power production vs. hub-height wind speed from the anemometer on the nacelle. The black line represents an approximation of the manufacturer power curve for the GE 1.5sle (GE Energy, 2009). Wind speed is normalized for density following IEC 61400-12-1 (2015). The grey dashed line marks rated speed.
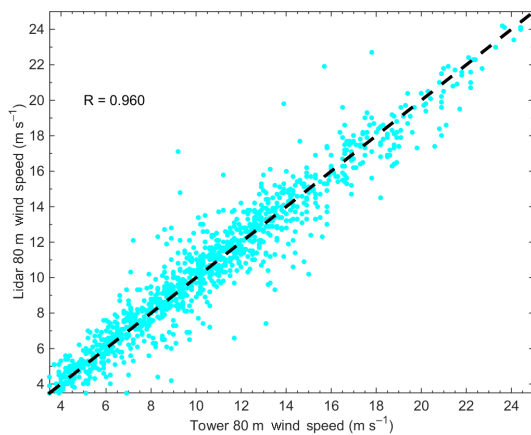

Figure 8. Lidar 80 m wind speeds compared to tower 80 m wind speeds filtered for wind speeds between 3.5 and 25.0 m s^{-1}, wind directions between 235 and 315°, and for normal turbine operation. Black dashed line represents a 1 : 1 relationship.

Aitken et al., 2014) to cause us to discuss and show only the upwind data from the tower from this point forward. Note, however, that not all sites are subject to the inhomogeneity seen at the NWTC, and all instruments available for wind measurement should be considered. Concurrent met tower and turbine data that fulfill the screening criteria occurred during 2240 10 min periods, equivalent to about 373 h of data, which is more than twice the 180 h of data that the IEC 61400-12-1 (2015) standard recommends for power performance testing.

3.5 Atmospheric stability regimes

Numerous approaches are available for classifying the atmospheric stability of a given 10 or 30 min time period. Bulk Richardson number (R_B) calculations use temperature and wind speed differences from the lowest met tower measurement to the height of the top of the rotor disk to compare the buoyant production of turbulence to the wind-shear-generated mechanical production of turbulence (Stull, 1988) as

$$R_B = \frac{g \Delta T \Delta z}{\overline{T} \Delta U^2}, \tag{1}$$

where g is the gravitational constant 9.81 m s^{-2}, Δz is the change in height, ΔT is the change in 10 min averages of temperature across Δz, $\overline{T}$ is the mean temperature across Δz, and ΔU is the change in the 10 min averages of horizontal wind speed across Δz. Note that Eq. (1) does not consider wind direction variability because cup anemometer measurements provide only information about horizontal wind speed. Typical stability classifications based on R_B calculations are as follows: turbulent flow in unstable conditions when R_B is less than 0, laminar flow in stable conditions when R_B is greater than 0.25, and neutral conditions when R_B is between 0 and 0.25 (Stull, 1988). These stability classifications are similar to those used in previous work on stability effects on wind turbine fatigue and loading in Kelley (2011), and slightly different from the stability classifications used in Vanderwende and Lundquist (2012). The distribution of R_B calculated from the tower measurements for this campaign (Fig. 9), however, suggests that slightly different regimes, shown in Table 2, could be used to better represent the data at this site. Similar to the approach used in Aitken et al. (2014), the R_B distribution is split roughly into thirds to allow for less overlap between stable and unstable regimes. The uncertainty in R_B for these instruments over the measurement period is about 0.01; therefore, the R_B classifications used are larger than the uncertainty.

Obukhov length (L) is also a useful measure of atmospheric stability, relying on surface stresses as well as heat fluxes to estimate the height in the surface layer at which

Table 2. Defined stability regimes.

Stability class	R_B	L (m)	α
Unstable conditions	$R_B < -0.03$	$-1000 < L \leq 0$	$\alpha < 0.11$
Neutral conditions	$-0.03 < R_B < 0.03$	$|L| \geq 1000$	$0.11 < \alpha < 0.17$
Stable conditions	$R_B > 0.03$	$0 \leq L < 1000$	$\alpha > 0.17$
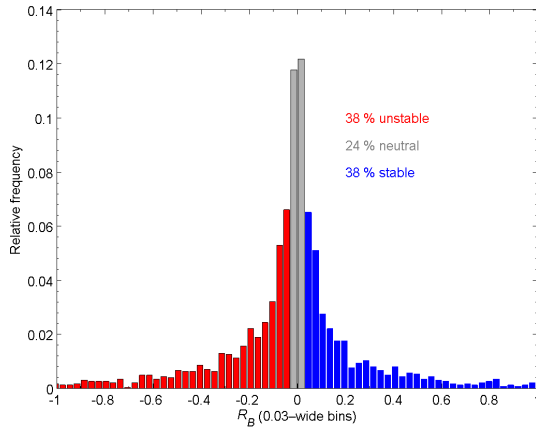
Figure 9. R_B distribution using thresholds in Table 2, including data filtered for tower 80 m wind speeds between 3.5 and 25.0 m s^{-1}, 87 m wind directions between 235 and 315°, and for normal turbine operation.
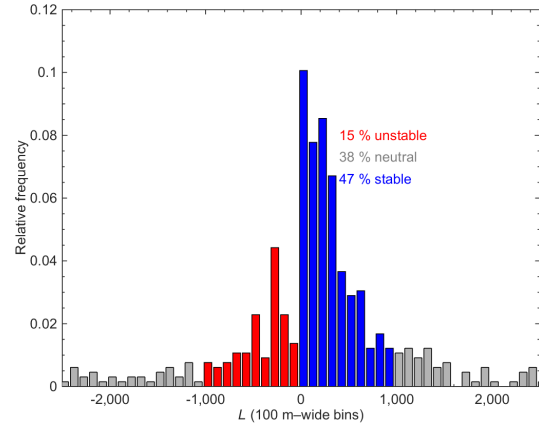
Figure 10. L distribution using thresholds in Table 2. Note that some neutral cases are outside of these axes. Includes data filtered for tower 80 m wind speeds between 3.5 and 25.0 m s^{-1}, 87 m wind directions between 235 and 315°, and for normal turbine operation.

the buoyant production of turbulence dominates wind-shear-generated mechanical production of turbulence (Stull, 1988) as

$$L = -\frac{u_*^3}{kg} \frac{T_v}{\overline{w'T_s'}}, \qquad (2)$$

where u_* is the friction velocity, k is the von Kármán constant 0.41, T_v is the virtual temperature, w' is the vertical wind speed fluctuation in the 30 min averaging period, and T_s' is the sonic temperature fluctuation in the 30 min averaging period. L calculations are based on sonic anemometer measurements at 15 m and temperature measurements interpolated to 15 m to ensure L is calculated using measurements within the surface layer. Typical stability classifications are used in this work and are based on L calculations as defined by Muñoz-Esparza et al. (2012), shown in Table 2. These classifications are slightly different from those used in Wharton and Lundquist (2012b). The distributions of L are shown in Fig. 10.

When the R_B and L stability approaches are compared against one another and against time of day, as in Fig. 11, the stability parameters differ slightly in their definitions of unstable and stable. Because of differences in stability classes due to varying approaches to defining atmospheric stability, we treat R_B-defined stability classes separately from L-defined stability classes in the power curves.

3.6 Turbulence regimes

TI can also be used to describe atmospheric conditions, as demonstrated by Rareshide et al. (2009), Wagenaar and Eecen (2011), and Wharton and Lundquist (2012a). TI is typically defined as

$$\text{TI} = \frac{\sigma_{80\,\text{m}}}{U_{80\,\text{m}}} \cdot 100, \qquad (3)$$

where $\sigma_{80\,\text{m}}$ is the 10 min standard deviation of the horizontal wind speed at 80 m and $U_{80\,\text{m}}$ is the 10 min mean horizontal wind speed at 80 m. Although the TI approach has been used successfully at other locations, the NWTC consistently features strong turbulence likely resulting from the terrain characteristics of the site (Figs. 12 and 13), making it difficult to distinguish typical stability classes from TI calculations. This strong ambient turbulence has led to the choice of site-specific turbulence classification defined in Table 3.

When the atmospheric stability regimes are compared to the TI regimes defined here (Fig. 14), the R_B and TI regime percentages also differ slightly in their definitions of unstable atmospheric conditions and highly turbulent conditions. Most of the daytime points are within the unstable regime as defined by R_B; however, only about 17 % of the data fall within unstable conditions with higher TI. This comparison, again, emphasizes the highly turbulent characteristics of the NWTC.
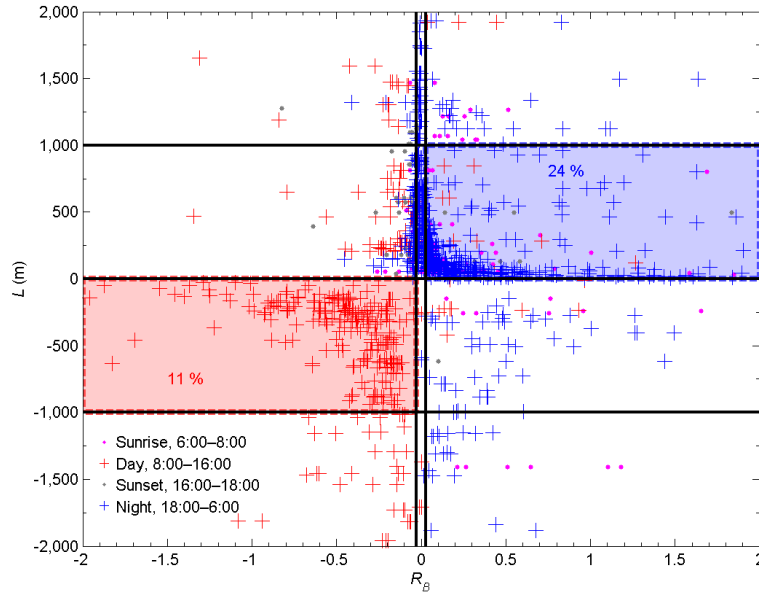
Figure 11. L vs. R_B. The blue box represents where both L and R_B agree on the stable conditions; the percentage (24 %) represents the percentage of data points in this box. The red box represents where both L and R_B agree on the unstable conditions; the percentage (11 %) represents the percentage of data points in this box. Includes data filtered for tower 80 m wind speeds between 3.5 and 25 m s^{-1}, 87 m wind directions between 235 and 315°, and for normal turbine operation.
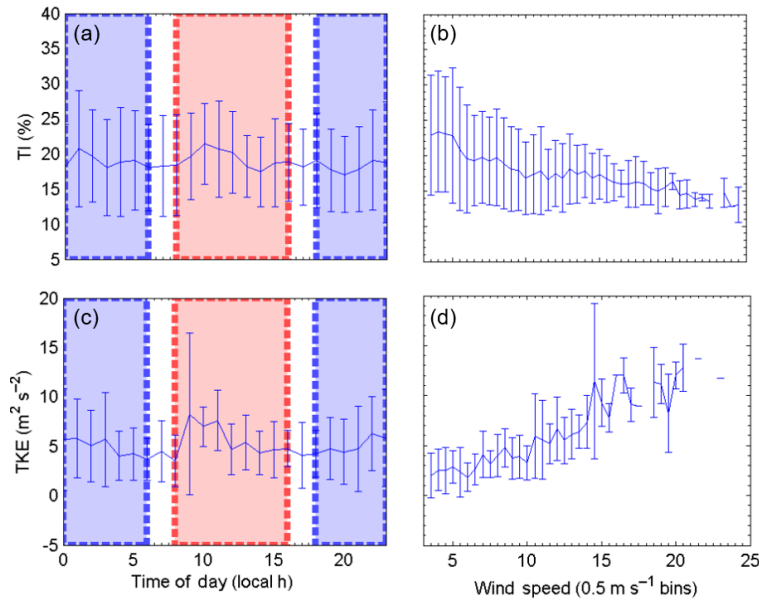

Figure 12. TI **(a)** and TKE **(c)** calculated with near-hub-height tower measurements vs. time of day, where hour 0 and hour 24 represent local midnight. The blue line represents the mean TI in the corresponding hour and the error bar represents the standard deviation. The blue rectangle represents nighttime hours and the red rectangle represents daytime hours. Mean and standard deviation of TI **(b)** and TKE **(d)** calculated with near-hub-height tower measurements in each wind speed bin. Includes data filtered for tower 80 m wind speeds between 3.5 and 25.0 m s^{-1}, 87 m wind directions between 235 and 315°, and for normal turbine operation.

To further understand the turbulence characteristics demonstrated during this campaign, we also calculate TKE using the 74 m 3-D sonic anemometer mounted on the M5 met tower. Although TI is a parameter typically calcu-lated and analyzed in the wind industry, TKE has the advantage of including the vertical component of the wind:
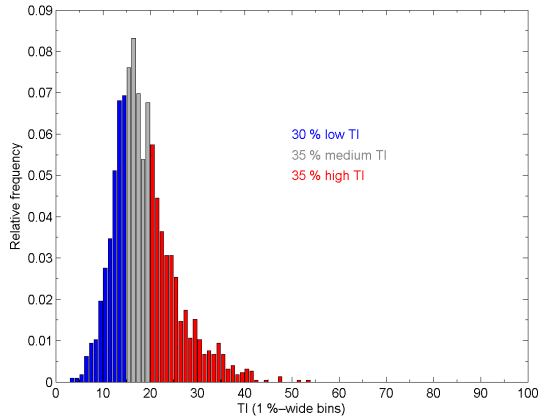
Figure 13. TI distribution using thresholds in Table 3. Includes data filtered for tower 80 m wind speeds between 3.5 and 25 m s^{-1}, 87 m wind directions between 235 and 315°, and for normal turbine operation.
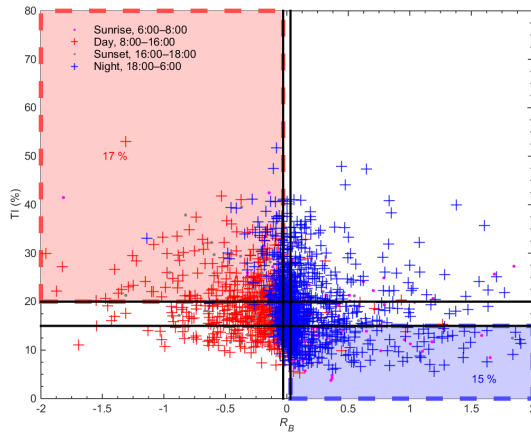

Figure 14. TI vs. R_B. The blue box represents where both TI and R_B agree on the stable conditions; the percentage (15 %) represents the percentage of data points in this box. The red box represents where both TI and R_B agree on the unstable conditions; the percentage (17 %) represents the percentage of data points in this box. Includes data filtered for tower 80 m wind speeds between 3.5 and 25 m s^{-1}, 87 m wind directions between 235 and 315°, and for normal turbine operation.

$$\text{TKE} = \frac{1}{2}\left(\overline{u'^2} + \overline{v'^2} + \overline{w'^2}\right), \tag{4}$$

where we calculate TKE per unit mass, u' is the perturbation from a 30 min average of the zonal component of the wind, v' is the perturbation from a 30 min average of the meridional component of the wind, and w' is the perturbation from a 30 min average of the vertical component of the wind. Using this TKE approach also reveals the strong turbulence at the NWTC, which is only slightly affected by the diurnal cycle during this wintertime campaign (Figs. 12 and 15). Turbulence classifications based on TKE are determined by the distribution in Fig. 15 and are listed in Table 3.

Table 3. Defined turbulence regimes.

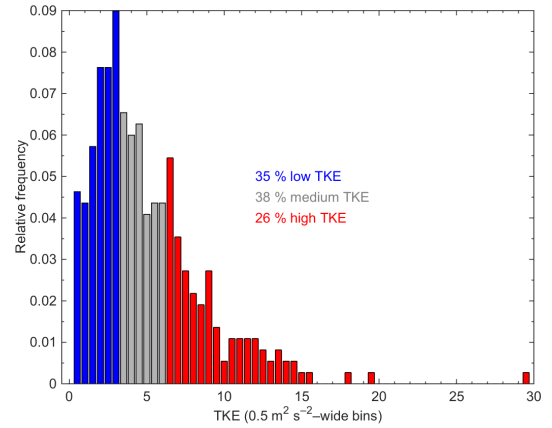| Turbulence regime	TI (%)	TKE (m^2 s^{-2})
High turbulence	TI > 20	TKE > 6.5
Medium turbulence	15 < TI < 20	3.0 < TKE < 6.5
Low turbulence	TI < 15	TKE < 3.0

Figure 15. TKE distribution using thresholds in Table 3. Includes data filtered for tower 80 m wind speeds between 3.5 and 25.0 m s^{-1}, 87 m wind directions between 235 and 315°, and for normal turbine operation.

Many cases with relatively high TI or TKE are considered neutral and stable according to our stability definitions in Table 3. Depending on whether TI, TKE, R_B, or L is considered as a measure of atmospheric stability, a particular time period may be classified differently. In other words, different results are found depending on the metric selected.

3.7 Wind shear regimes

To estimate the effect of the wind speed vertical profile across the rotor disk, the wind shear exponent or power law exponent parameter, α, is typically used in the wind energy industry:

$$\alpha = \frac{\log\left(\frac{U_2}{U_1}\right)}{\log\left(\frac{z_2}{z_1}\right)}, \tag{5}$$

where z_1 is the reference height, z_2 is the height above ground level, U_2 is the wind speed at height z_2, and U_1 is the wind speed at height z_1. At the NWTC during this study, the average wind shear exponent using the 122 and 38 m tower wind speeds as z_2 and z_1, respectively, is 0.15. The standard deviation is 0.14 and the maximum wind shear exponent is 1.10.

For this period of time at this site, however, it was rare for the rotor equivalent wind speed (REWS) to deviate significantly from the hub-height wind speed (Sect. S2). There-

fore, shear exponents are separated into regimes simply by splitting the shear exponent distribution into thirds (Table 2, Fig. 16). Other approaches to classify stability regimes using shear exponents such as combining with other stability measures such as L and R_B (Vanderwende and Lundquist, 2012), or using a REWS in the power curves (Elliott and Cadogan, 1990), may work at other sites.

4 Results

To explore the variability in the power curves, we apply filters to the power curves based on factors such as atmospheric stability and TI. We apply a new method to calculate AEP using these classifications. We can consider periods with low TI to be approximately "stable" by R_B and L; "unstable" conditions would generally have high TI. Our results show that, generally, at this site with little veer, stable conditions (with varying degrees of significance) lead to over-performance at wind speeds just below rated power. At lower wind speeds, however, unstable conditions lead to over-performance.

4.1 Power curves

The NWTC site generally exhibits high TI throughout this data collection period. Even so, some differences in power produced emerge at wind speeds between 5 and $7\,\mathrm{m\,s^{-1}}$ and at wind speeds between 10 and $14\,\mathrm{m\,s^{-1}}$ after separating the TI into relative classes of low, medium, and high TI (Figs. 17a, c and 18a, c, Table 3). Statistically distinct differences within each wind speed bin between the TI classes defined in Table 3 are determined by the Wilcoxon rank sum test with a 1 % significance level. These statistically distinct bins are denoted by closed circles in Figs. 17a, c and 18a, c. This statistical test shows that, for the power curves using nacelle winds, periods of relatively high TI produce significantly more power than periods of relatively low TI at wind speeds between 5 and $9\,\mathrm{m\,s^{-1}}$ (Figs. 17a and 18a). For the power curves using upwind tower winds, periods of relatively high TI produce significantly more power than periods of relatively low TI at wind speeds between 6.0 and $6.5\,\mathrm{m\,s^{-1}}$ (Figs. 17c and 18c). Conversely, power curves using nacelle winds show that, at wind speeds between 10.5 and $13.5\,\mathrm{m\,s^{-1}}$, periods of relatively low TI produce significantly more power than periods of relatively high TI. Power curves using upwind tower winds show that, at wind speeds between 9.5 and $15.5\,\mathrm{m\,s^{-1}}$, periods of relatively low TI produce significantly more power than periods of relatively high TI. Rareshide et al. (2009) found similar behavior.

On the other hand, power curves separated by R_B-defined stability class show only a few bins that are statistically distinct in power produced (Figs. 17b, d and 18b, d). Power curves using nacelle winds show that, at most wind speeds between 6.5 and $9.0\,\mathrm{m\,s^{-1}}$, periods of unstable conditions produce significantly more power than periods of stable conditions. Power curves using upwind tower winds show that,
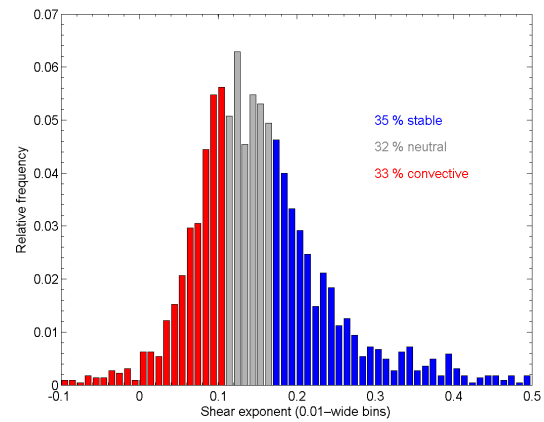

Figure 16. Shear exponent distribution using thresholds in Table 2. Includes data filtered for tower 80 m wind speeds between 3.5 and $25.0\,\mathrm{m\,s^{-1}}$, 87 m wind directions between 235 and 315°, and for normal turbine operation.

at wind speeds around $7\,\mathrm{m\,s^{-1}}$, periods of unstable conditions produce significantly more power than periods of stable conditions. Power curves using both nacelle winds and tower winds show that, at wind speeds around $12\,\mathrm{m\,s^{-1}}$, periods of stable conditions produce significantly more power than periods of unstable conditions.

Distinct differences between power curves calculated from nacelle winds and power curves calculated from upwind tower winds occur in the power curves of both of these atmospheric parameters. Statistically distinct wind speed bins in power curves calculated from nacelle winds tend to be similar to those in power curves calculated from tower winds near rated speed. At lower wind speeds, however, between about 5 and $9\,\mathrm{m\,s^{-1}}$, many more statistically distinct differences emerge between nacelle power curves than between tower power curves, most notably in the power curves segregated by TI regimes. Turbine operations are especially variable in this region of rapid increase in power with wind speed. The turbine reacts directly to the conditions as measured by instruments on the turbine. The nacelle-mounted anemometer observes winds that flow through the rotor disk and along the nacelle during turbine operation, and therefore likely measures different wind speeds than the upwind met tower. The nacelle anemometer observes complex flows behind the rotor disk that are strongly influenced by ambient turbulence, leading to more statistically significant differences in the nacelle power curves for TI regimes.

Agreement between the TI and R_B methods means that at wind speeds around rated, low TI and high stability result in over-performance relative to high TI and low stability. Both methods also agree that somewhere in between cut-in and rated, sometimes called "region 2", high TI and low stability result in over-performance relative to low TI and high stability. Power curves separated by L-defined stability class as well as power curves separated by shear class do not show
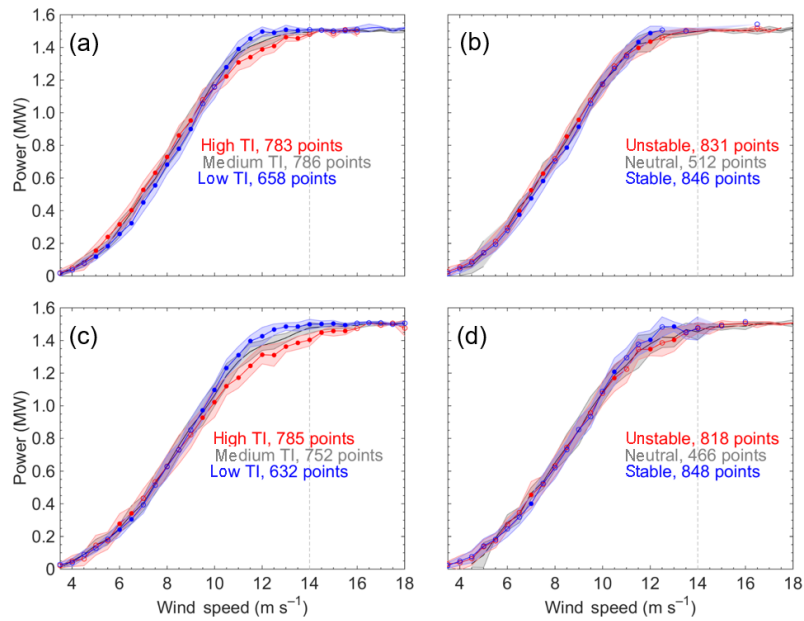
Figure 17. Nacelle anemometer power curves with **(a)** TI regimes and **(b)** R_B regimes. Eighty-meter tower anemometer power curves with **(c)** TI regimes and **(d)** R_B regimes. Median statistics are used to avoid outlier effects. Statistically distinct differences within each wind speed bin between the regimes are determined by the Wilcoxon rank sum test with a 1 % significance level and denoted by closed circles. Includes data filtered for tower 80 m wind speeds between 3.5 and 25.0 m s^{-1}, 87 m wind directions between 235 and 315°, and for normal turbine operation. Envelopes represent ±1 MAD for each wind speed bin. The grey dashed line marks rated speed.
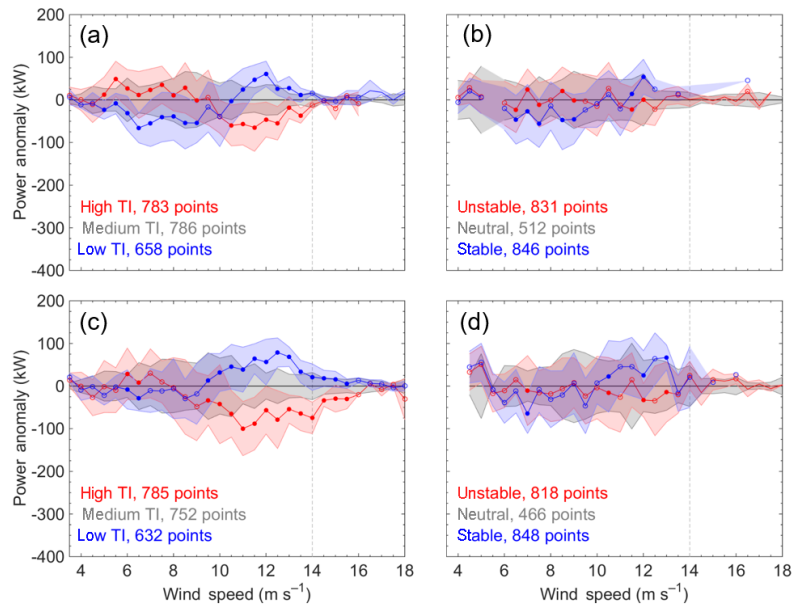

Figure 18. Nacelle anemometer power curves shown as the anomaly from the neutral or medium power curve of the **(a)** TI regimes and **(b)** R_B regimes. Eighty-meter tower anemometer power curves shown as the anomaly from the neutral or medium power curve of the **(c)** TI regimes and **(d)** R_B regimes. Median statistics are used to avoid outlier effects. Statistically distinct differences within each wind speed bin between the regimes are determined by the Wilcoxon rank sum test with a 1 % significance level and denoted by closed circles. Includes data filtered for tower 80 m wind speeds between 3.5 and 25.0 m s^{-1}, 87 m wind directions between 235 and 315°, and for normal turbine operation. Envelopes represent ±1 MAD for each wind speed bin. The grey dashed line marks rated speed.

any statistically significant differences in power produced between unstable and stable periods (not shown). Power curves separated by TKE class show few statistically significant differences in power produced between high and low TKE periods, likely because of the few data points available for the 30 min averaging period; therefore, these results are shown in the Supplement (Sect. S4).

The large variability reported in the literature (and herein) regarding power production can be understood by recognizing the interactions between a pitch-controlled turbine and the atmosphere: the operation of control algorithms changes with wind speed, with varying effects depending on the ambient turbulence.

Sensitivity to atmospheric turbulence occurs at low wind speeds, near cut-in wind speed. In these conditions, the turbine generator speed (revolutions per minute, RPM) increases, as does the generator torque. As a result, the blades will often pitch backward, changing the angle of attack to generate more lift, and the power production ramps up. At low wind speeds and higher turbulence, the turbine can react to the higher variation in wind speed and can capitalize on the variation seen in the wind flow because of the additional lift resulting from the blade pitch, and the turbine produces more power. Conversely, at low wind speeds with lower turbulence, the variation in wind speed is lower, and so the turbine experiences more consistent wind than in highly turbulent conditions and therefore produces less power.

At higher wind speeds, closer to or just below rated speed, control mechanisms seek to maintain rated generator speed, rather than continuing to increase generator speed. The blades will pitch forward (or "feather"), allowing the power production to maintain rated power. This process effectively decreases the amount of lift when compared to lift generated by a non-feathered blade. At these wind speeds during periods of high TI, a turbine reacts to the high variation in wind speed with subtle changes in blade pitch. For example, if the turbine detects a drop in wind speed, the blades may pitch back to generate more lift, but then if the wind speed increases quickly after, the blades will pitch forward again. If the blade pitch cannot immediately respond to increases in wind speed, then power losses occur. At these higher wind speeds, lower turbulence enables consistent blade pitch to match atmospheric conditions, and so the turbine can capture more power.

It is also important to mention the strong connection between turbulence and shear: high shear will eventually erode turbulence (Wharton and Lundquist, 2012a). Periods of high shear generally coincide with periods of low turbulence and vice versa. With low shear, the mean wind speed is more consistent over the height of the rotor disk. However, since we did not see significant differences in power curves for different shear regimes here, we cannot speculate further on this in this analysis. Finally, if veer occurs in the wind profile (as in Vanderwende and Lundquist, 2012, and Dörenkamper et al., 2014), which usually occurs only in stable or low turbulence

Table 4. Weibull parameters for the case of no stability or turbulence filter as well as for each turbulence and stability class.

	Scale parameter	Shape parameter	Mean
No filter	10.04	2.63	8.90
Low TI regime	10.83	2.59	9.60
Med TI regime	10.81	2.90	9.63
High TI regime	8.52	2.81	7.57
Low R_B regime	10.12	3.09	9.05
Med R_B regime	13.29	3.45	11.96
High R_B regime	7.64	3.10	6.83

atmospheric conditions, that veer will generally undermine power production as the turbine blades are not oriented perpendicular to the flow at all vertical levels.

4.2 Annual energy production

AEP allows developers and operators to quantify the projected energy production of a turbine. To quantify the impact on AEP of these stability- and turbulence-driven differences in power curves, we use a Weibull distribution for wind speed and calculate AEP with no filter, as well as with TI and stability filters. These turbulence and stability filters for the AEP calculations can be further explained as AEP calculated using the power curves calculated from nacelle winds (Fig. 17a and b) as well as the power curves calculated from upwind tower winds (Fig. 17c and d). These power curves are used together with a sample wind distribution using Weibull distribution parameters based on wind speed data separated into each stability class (Table 4) as suggested by IEC 61400 12-1 (2015) for a site-specific AEP. For each of these filters, separate AEP calculations are made for each regime, weighted by the number of data points in that regime, and then added together to compare with the AEP calculated with no atmospheric filter. Note that although data are collected only during 2.5 months in the winter of 2012, AEP is calculated for an entire year to show values closer to a representative AEP value.

Results in Table 5 show a higher AEP when using no filter, followed by an AEP calculated with a TI filter and then a stability filter. The lower AEP calculated when separating by stability and turbulence regimes suggests that the AEP calculated using no filters may be overestimating the production, perhaps because the higher and lower extremes of the parameter ranges bias the averages in each bin.

AEP results in Table 5 also show that the AEP calculated using nacelle winds underestimates the AEP when compared with an AEP calculated using upwind tower measurements. This underestimation of the nacelle anemometer-calculated AEP is true for both the AEP calculated for the entire data set as well as with each stability or turbulence filter and is likely because the nacelle anemometer underestimates the ambient

Table 5. AEP in megawatt-hours per year calculated for different atmospheric and turbulence regimes using a Weibull distribution with a scale and shape parameter associated with the corresponding wind speed distribution.

	No filter	TI filter	R_B filter
AEP using tower data	7479.3	7409.6	7278.7
AEP using nacelle data	7430.6	7388.9	7266.7

Table 6. AEP in percentage calculated for different filter regimes using a Weibull distribution with a scale factor and a shape factor representative of the corresponding wind speed distribution. Medium regime is set at 100 % and low and high regimes are percentages compared to the medium regime. The highest value within each row is italicized.

Filter	Low regime	Medium regime	High regime
TI using tower data	85.03	*100.00*	68.20
R_B using tower data	*116.28*	100.00	71.33
TI using nacelle data	84.76	*100.00*	68.32
R_B using nacelle data	*115.86*	100.00	70.52

wind speed due to flow interference of the rotor disk and nacelle.

When the AEP's low and high regimes are compared to the medium regimes of their respective atmospheric parameters, the AEP for medium-TI periods is higher than that for low-TI periods and for high-TI periods for both the nacelle anemometer-calculated AEP and the tower-calculated AEP (Table 6). Using low- and high-TI power curves results in an AEP smaller than that calculated using the medium-TI power curve. These results are likely obtained because the low-TI power curve loses production at lower wind speeds and the high-TI power curve loses production around rated speed. When using a stability filter, the AEP calculated with the low-R_B power curve is higher than that with the high-R_B power curve (Table 6). This contrast between AEP calculated for the low-stability regime and AEP calculated for the high-stability regimes suggests that the unstable power curve (Fig. 17b and d) gains enough production at lower wind speeds to surpass the production gain by the stable power curve (Fig. 17b and d) near rated wind speed.

5   Conclusions

Using 2.5 months of data from upwind and nacelle-based instruments, we calculate power curves for different regimes of atmospheric stability and turbulence as well as AEP with and without these atmospheric filters. This work not only focuses on the idea of calculating different power curves for different atmospheric conditions for power performance testing but also highlights the differences in AEP that can emerge from the application of stability- or turbulence-dependent power curves. We also summarize extensive data quality-control methods, including two approaches for filtering out turbine underperformance or curtailments.

Statistically significant differences emerge among power curves segregated by TI and R_B. At wind speeds between 5 and 7 m s^{-1}, during periods of high TI, significantly more power is produced than during periods of low TI. From about 10 to 14 m s^{-1} (near rated wind speed), during periods of low TI, significantly more power is produced than during periods of high TI. During periods of stable conditions, significantly more power is produced than during periods of unstable conditions around 12 m s^{-1}, and significantly less power is produced than during periods of unstable condi-

tions at some wind speeds between 6.5 and 9.0 m s^{-1}. Statistically significant distinctions in power curves did not occur when filtering for TKE, L, yaw error, wind shear, or wind veer for this data set at this site, perhaps explaining why stable conditions promote overperformance here, as in Wharton and Lundquist (2012b). A site with veer, however, exhibits underperformance in stable conditions (Vanderwende and Lundquist, 2012).

After calculating an AEP for each regime and comparing the high and low regimes with the medium regime, differences between AEP calculated using different atmospheric filters are revealed. An AEP calculated with no atmospheric or turbulence filter is higher than any AEP calculated with these filters. In addition, the AEP calculated using a TI filter shows that the AEP calculated with the medium TI regime is greater than the AEP calculated with the low or high TI regimes. The AEP calculated with the R_B filter shows that the low-regime AEP is much larger than the AEP in the high and medium regimes.

As a small percent difference in AEP leads to a large deviation in cost for both operators and manufacturers, calculating different power curves for different atmospheric conditions may not only be a practical approach but may also lower the financial risks for both operators and manufacturers.

As discussed by Rareshide et al. (2009), manufacturers increasingly filter out data that represent what they consider anomalous or extreme atmospheric conditions for power performance testing. The IEC-61400-12-1 (2015) standard calls for at least 180 h of data to be used in a power performance test. Consequently, if manufacturers filter out data based on higher TI values, for instance, this means that more data must be gathered to make up for the discarded data. We see this discarding of data as unnecessary and potentially more costly. We suggest that instead of discarding these data, different power curves be calculated for different conditions. This approach can allow for a more nuanced understanding of how a turbine operates in different atmospheric conditions, and may lead to a more accurate and reliable performance result and AEP calculation.

6 Data availability

Data from the M5 tower are available for download at http://wind.nrel.gov/MetData/135mData/M5Twr/.

References

Aitken, M. L., Rhodes, M. E., and Lundquist, J. K.: Performance of a wind-profiling lidar in the region of wind turbine rotor disks, J. Atmos. Ocean. Tech., 29, 347–355, doi:10.1175/JTECH-D-11-00033.1, 2012.

Aitken, M. L., Lundquist, J. K., Pichugina, Y. L., and Banta, R. M.: Quantifying wind turbine wake characteristics from scanning remote sensor data, J. Atmos. Ocean. Tech., 31, 765–787, doi:10.1175/JTECH-D-13-00104.1, 2014.

Antoniou, I. and Pedersen, T. F.: Nacelle Anemometry on a 1MW Wind Turbine, Risø National Laboratory, Roskilde, Denmark, 37 pp., 1997.

Antoniou, I., Pedersen, S. M., and Enevoldsen, P. B.: Wind shear and uncertainties in power curve measurement and wind resources, Wind Eng., 33, 449–468, doi:10.1260/030952409790291208, 2009.

Banta, R. M., Oliver, L. D., Gudiksen, P. H., and Lange, R.: Implications of small-scale flow features to modeling dispersion over complex terrain, J. Appl. Meteorol., 35, 330–342, 1996.

Bingöl, F., Mann, J., and Foussekis, D.: Conically scanning LIDAR error in complex terrain, Meteorol. Z., 18, 189–195, doi:10.1127/0941-2948/2009/0368, 2009.

Choukulkar, A., Pichugina, Y., Clack, C. T. M., Calhoun, R., Banta, R., Brewer, A., and Hardesty, M.: A new formulation for rotor equivalent wind speed for wind resource assessment and wind power forecasting, Wind Energy, 19, 1439–1452, doi:10.1002/we.1929, 2016.

Clifton, A.: Remote sensing of complex flows by Doppler wind lidar: issues and preliminary recommendations, NREL, Golden, Colorado, 1–42, 2015.

Clifton, A. and Lundquist, J. K.: Data clustering reveals climate impacts on local phenomena, J. Appl. Meteorol. Clim., 51, 1547–1557, doi:10.1175/JAMC-D-11-0227.1, 2012.

Clifton, A., Kilcher, L., Lundquist, J. K., Fleming, P.: Using machine learning to predict wind turbine power output, Environ. Res. Lett., 8, 024009, doi:10.1088/1748-9326/8/2/024009, 2013a.

Clifton, A., Schreck, S., Scott, G., and Lundquist, J. K.,: Turbine inflow characterization at the National Wind Technology Center, J. Sol. Energ.-T. ASME, 135, 031017, doi:10.1115/1.4024068, 2013b.

Courtney, M., Wagner, R., and Lindelöw, P.: Testing and comparison of LIDARs for profile and turbulence measurements in wind energy, IOP Conf. Ser. Earth Environ. Sci., 1, 1–14, doi:10.1088/1755-1307/1/1/012021, 2008.

Dörenkämper, M., Tambke, J., Steinfeld, G., Heinemann, D., and Kühn, M.: Atmospheric impacts on power curves of multi-megawatt offshore wind turbines, J. Phys. Conf. Ser., 555, 1–11, doi:10.1088/1742-6596/555/1/012029, 2014.

Elliott, D. L. and Cadogan, J. B.: Effects of wind shear and turbulence on wind turbine power curves, Proc. European Community Wind Energy Conference and Exhibition, Madrid, Spain, 1990.

Frandsen, S., Sørensen, J. N., Mikkelsen, R., Pederesen, T. F., Antoniou, I., and Hansen, K.: The generics of wind turbine nacelle anemometry, Proceedings of European Wind Energy Conference, Marseille, France, 2009.

GE Energy: 1.5 MW wind turbine, http://geosci.uchicago.edu/~moyer/GEOS24705/Readings/GEA14954C15-MW-Broch.pdf (last access: 21 January 2013), 2009.

Gottschall, J. and Peinke, J.: How to improve the estimation of power curves for wind turbines, Environ. Res. Lett., 3, 1–7, doi:10.1088/1748-9326/3/1/015005, 2008.

Hunter, R., Pedersen, T. F., Dunbabin, P., Antoniou, I., Frandsen, S., Klug, H., Albers, A., and Lee, W. K.: European wind turbine testing procedure developments: Task 1: measurement method to verify wind turbine performance characteristics, Risø National Laboratory, Roskilde, Denmark, 1–120, 2001.

IEC 61400-12-1 Ed 2.0: Wind turbines – Part 12-1: power performance measurements of electricity producing wind turbines, IEC, Geneva, Switzerland, 2015.

Kaiser, K., Hohlen, H., and Langreder, W.: Turbulence correction for power curves, Wind Energy Proc. European Wind Energy Conference and Exhibition, Madrid, 159–162, 2003.

Kelley, N. D.: Turbulence-turbine interaction: the basis for the development of the TurbSim Stochastic Simulator, NREL, Golden, Colorado, http://www.nrel.gov/docs/fy12osti/52353.pdf (last access: 8 May 2016), 2011.

Lundquist, J. K., Churchfield, M. J., Lee, S., and Clifton, A.: Quantifying error of lidar and sodar Doppler beam swinging measurements of wind turbine wakes using computational fluid dynamics, Atmos. Meas. Tech., 8, 907–920, doi:10.5194/amt-8-907-2015, 2015.

Mendoza, I., Hur, J., Thao, S., Curtis, A.: Power performance test report for the U.S. Department of Energy 1.5-megawatt wind turbine, NREL, Golden, Colorado, 1–55, http://www.nrel.gov/docs/fy15osti/63684.pdf (last access: 8 May 2016), 2015.

Motta, M., Barthelmie, R. J., and Vølund, P.: The influence of non-logarithmic wind speed profiles on potential power output at Danish offshore sites, Wind Energy, 8, 219–236, 2005.

Muñoz-Esparza, D., Cañadillas, B., Neumann, T., and vanBeech, J.: Turbulent fluxes, stability and shear in the offshore environment: mesoscale modelling and field observations at FINO1, J. Renew. Sustain. Energy, 4, 1–16, doi:10.1063/1.4769201, 2012.

NWTC: 135-m Tower Data, https://nwtc.nrel.gov/MetData, last access: 18 May 2016.

Poulos, G. S., Bossert, J. E., Pielke, R. A., and McKee, T. B.: The interaction of katabatic flow and mountain waves I: observations and idealized simulations, J. Atmos. Sci., 57, 1919–1936, 2000.

Poulos, G. S., Bossert, J. E., Pielke, R. A., and McKee, T. B.: The interaction of katabatic flow and mountain waves II: case study analysis and conceptual model, J. Atmos. Sci., 64, 1857–1879, 2007.

Rareshide, E., Tindal, A., Johnson, C., Graves, A. M., Simpson, E., Bleeg, J., Harris, T., and Schoborg, D.: Effects of complex wind regimes on turbine performance, AWEA Windpower 2009 meeting, Chicago, Illinois, 2009.

Rhodes, M. E. and Lundquist, J. K.: The effect of wind-turbine wakes on summertime US Midwest atmospheric wind profiles as observed with ground-based Doppler LIDAR, Bound.-Lay. Meteorol. 149, 85–103, doi:10.1007/s10546-013-9834-x, 2013.

Rinker, J. M., Gavin, H. P., Clifton, A., Veers, P. S., and Kilcher, L. F.: Temporal coherence: a model for non-stationarity in natural and simulated wind records, Bound.-Lay. Meteorol., 159, 373–389, doi:10.1007/s10546-015-0121-x, 2016.

Smith, B., Link, H., Randall, G., and McCoy, T.: Applicability of Nacelle Anemometer Measurements for Use in Turbine Power Performance Tests, AWEA Windpower, Portland, OR, 2002.

Stull, R. B.: An Introduction to Boundary Layer Meteorology, Kluwer Academic Publishers, the Netherlands, 1988.

Sumner, J. and Masson, C.: Influence of atmospheric stability on wind turbine power performance curves, J. Sol. Energ.-T. ASME, 128, 531–538, doi:10.1115/1.2347714, 2006.

van den Berg, G. P.: Wind turbine power and sound in relation to atmospheric stability, Wind Energy, 11, 151–169, 2008.

Vanderwende, B. and Lundquist, J. K.: The modification of wind turbine performance by statistically distinct atmospheric regimes, Environ. Res. Lett., 7, 1–7, doi:10.1088/1748-9326/7/3/034035, 2012.

Wagenaar, J. W. and Eecen, P. J.: Dependence of power performance on atmospheric conditions and possible corrections, European Wind Energy Association (EWEA) 2011 conference, Brussels, Belgium, http://www.ecn.nl/docs/library/report/2011/m11033.pdf (last access: 9 May 2016), 2011.

Wagner, R., Antoniou, I., Pedersen, S., Courtney, M., and Jorgensen, H.: The influence of the wind speed profile on wind turbine performance measurements, Wind Energy, 12, 348–362, doi:10.1002/we.297, 2009.

Wharton, S. and Lundquist, J. K.: Atmospheric stability affects wind turbine power collection, Environ. Res. Lett., 7, 1–9, doi:10.1088/1748-9326/7/1/014005, 2012a.

Wharton, S. and Lundquist, J. K.: Assessing atmospheric stability and its impacts on rotor-disk wind characteristics at an onshore wind farm, Wind Energy, 15, 525–546, doi:10.1002/we.483, 2012b.

Zahle, F. and Sørensen, N. N.: Characterization of the unsteady flow in the nacelle region of a modern wind turbine, Wind Energy, 13, 271–283, doi:10.1002/we.418, 2011.